



# Continuous monitoring of a trapped superconducting spin

M. Hays<sup>1</sup>✉, V. Fatemi<sup>1</sup>✉, K. Serniak<sup>1</sup>, D. Bouman<sup>2</sup>, S. Diamond<sup>1</sup>, G. de Lange<sup>1,3</sup>, P. Krogstrup<sup>4</sup>, J. Nygård<sup>4</sup>, A. Geresdi<sup>2</sup> and M. H. Devoret<sup>1</sup>✉

**Readout and control of electrostatically confined electrons in semiconductors are key primitives of quantum information processing with solid-state spin qubits<sup>1,2</sup>. In semiconductor–semiconductor heterostructures, localized electronic modes known as Andreev levels result from confinement that is provided by the pair potential<sup>3,4</sup>. Unlike electronic modes confined exclusively via electrostatic effects, Andreev levels carry supercurrent. Therefore, they naturally integrate with the techniques of circuit quantum electrodynamics (cQED) that have been developed in the field of superconducting qubits and used to detect pairs of quasiparticles that are trapped in Andreev levels<sup>5–8</sup>. Here, we demonstrate single-shot cQED readout of the spin of an individual quasiparticle trapped in the Andreev levels of a semiconductor nanowire Josephson element. Owing to a spin-orbit interaction in the nanowire, this ‘superconducting spin’ directly determines the flow of supercurrent through the element. We harnessed this spin-dependent supercurrent to achieve both a zero-field spin splitting and a long-range interaction between the quasiparticle and a superconducting microwave resonator<sup>9–13</sup>. Measurement of the resultant spin-dependent resonator frequency yielded quantum non-demolition spin readout with 92% fidelity in 1.9  $\mu\text{s}$ , which enabled us to monitor the quasiparticle spin in real time. These results pave the way for superconducting spin qubits that operate at zero magnetic field and for time-domain measurements of Majorana zero modes<sup>9,10,12,14,15</sup>.**

Superconducting circuits provide an important set of tools for the creation, manipulation, and measurement of quantum systems. In circuit quantum electrodynamics (cQED)<sup>5,6</sup>, a quantum system of interest is coupled to a superconducting resonator such that the resonator frequency depends on the system state. By combining superconducting quantum-limited amplifiers<sup>16</sup> with standard microwave technology, the system state can be detected non-destructively with near-unity single-shot fidelity. However, integration of this hardware with single quantum spins is complicated by the inherently weak interaction between the electron magnetic dipole moment and magnetic fields. It is therefore necessary to couple the spin to the resonator electromagnetic field through an intermediary degree of freedom that interacts with both systems<sup>17–26</sup>. A natural candidate for the mediator is the relativistic coupling between spin and translational degrees of freedom known as spin-orbit interaction. This has been used in semiconductor quantum dots to couple the electron spin to a resonator electric field through the electric dipole moment of the dot charge states<sup>17</sup>, but such schemes are constrained

by limited dot sizes. Here, we demonstrate a fundamentally different approach by inductively coupling to the spin-dependent supercurrent of a semiconductor nanowire Josephson element (also known as a Josephson nanowire), which has no such limitation.

A Josephson element composed of a semiconductor nanowire that connects two superconducting reservoirs hosts discrete fermionic modes known as Andreev levels, which can be occupied through spin-1/2 quasiparticle excitations<sup>3,4</sup>. While a quasi-electron completely confined to a dot cannot participate in charge transport, the quasiparticle that occupies the Andreev levels directly determines the flow of supercurrent through the Josephson nanowire. Even though the Andreev levels are localized at the junction, the supercurrent can extend over macroscopic distances that are limited by only the circuit geometry, and therefore the Andreev levels can be strongly coupled to a superconducting resonator<sup>7,8</sup>. Recently, theoretical<sup>9–12</sup> and experimental<sup>13</sup> work has shown that a Josephson nanowire with an appropriate spin-orbit interaction hosts spin-split Andreev levels and therefore spin-dependent supercurrent. In our study, we combine the fields of confined spins and cQED by detecting the spin state of a quasiparticle trapped in the Andreev levels of a Josephson nanowire. By inductively coupling the quasiparticle to a superconducting microwave resonator through the spin-dependent supercurrent, we achieve single-shot quantum non-demolition (QND) readout of the quasiparticle spin.

We first present a qualitative picture of the Andreev levels that are hosted by Josephson nanowires<sup>8,13,27</sup>, which have been developed by proximitizing semiconductor nanowires with superconducting contacts. Andreev levels can be understood as the bound states of a finite square well, with the barriers provided by the superconducting pair potential  $\Delta$  of the two superconducting reservoirs (Fig. 1a). Quasi-electrons (quasi-holes) that propagate in the nanowire between the reservoirs are Andreev-reflected into quasi-holes (quasi-electrons) upon reaching these barriers, a process that conserves the particle spin, the particle energy, and approximately the particle momentum but injects a charge of  $-2e$  ( $+2e$ ) into the reservoir (Fig. 1b). Localized, spectrally sharp levels form when the quantum mechanical phases that accumulate during a round-trip of propagation and Andreev reflections interfere constructively. These levels are usually paired into spin-degenerate doublets, and the number of doublets increases with both the number of conduction channels and the length  $\ell$  of the weak link.

In this study, the device was fabricated from an indium arsenide (InAs) nanowire that was partially covered in epitaxial Al, with a weak link formed by an  $\ell \approx 500$  nm uncovered section (Fig. 1e). For such a link, the chemical potential in the nanowire can be tuned

<sup>1</sup>Department of Applied Physics, Yale University, New Haven, CT, USA. <sup>2</sup>QuTech and Kavli Institute of Nanoscience, Delft University of Technology, Delft, The Netherlands. <sup>3</sup>Microsoft Quantum Lab Delft, Delft, The Netherlands. <sup>4</sup>Center for Quantum Devices, Niels Bohr Institute, University of Copenhagen, Copenhagen, Denmark. ✉e-mail: [max.hays@yale.edu](mailto:max.hays@yale.edu); [valla.fatemi@yale.edu](mailto:valla.fatemi@yale.edu); [michel.devoret@yale.edu](mailto:michel.devoret@yale.edu)

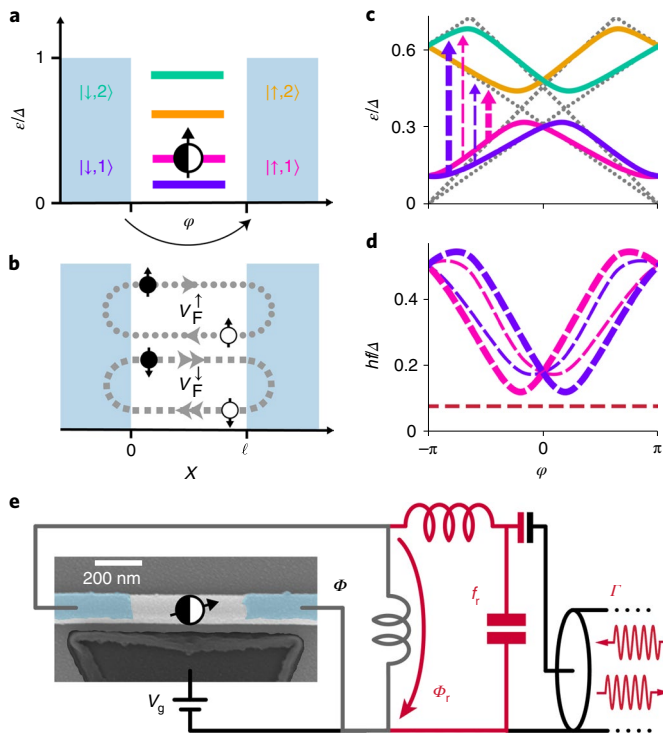


**Fig. 1 | Spin-orbit split Andreev levels coupled to a microwave resonator.**

**a**, One quasiparticle is trapped in a Josephson nanowire, where it is restricted to two doublets of Andreev levels. **b**, Owing to spin-orbit coupling, charge carriers traverse the weak link with a spin-dependent Fermi velocity  $v_F^s$ . Upon reaching a superconducting reservoir, quasi-electrons (black) are Andreev-reflected into quasi-holes (white), and vice versa. Levels form when these processes interfere constructively. The y axis does not represent a physical quantity. **c**, For a perfectly ballistic channel, the level energies have a linear  $\varphi$  dispersion that scales with  $v_F^s$  (grey dotted lines). Crossings at  $\varphi = 0, \pi$  are protected by time-reversal symmetry, but other crossings are avoided owing to normal scattering. Transitions out of  $|\downarrow, 1\rangle$  ( $|\uparrow, 1\rangle$ ) are indicated by purple (pink) dashed arrows, with thin or thick lines to denote whether the spin is flipped or maintained, respectively. **d**, Microwave transition frequencies  $f$  as a function of  $\varphi$ , with color and weight matching the arrows shown in **c**. Maroon line denotes resonator transition. **e**, Colour-enhanced scanning electron micrograph of a Josephson nanowire similar to the experimental device (see Methods). The InAs nanowire was partially coated by epitaxial Al (blue), with an uncovered region that formed the weak link. A flux  $\Phi$  applied through a small-inductance loop set the weak-link phase bias  $\varphi \simeq 2\pi \frac{\Phi}{\Phi_0} \text{mod}(2\pi)$ . The gate voltage  $V_g$  was used to tune the nanowire such that only two doublets were observed ( $V_g = -1.36$  V for all data presented in the main text). The Josephson nanowire was inductively coupled to a superconducting resonator (red, frequency  $f_r = 9.188$  GHz), which was coupled to a transmission line to probe the reflection amplitude  $\Gamma$ .

such that two doublets are present. In the excitation picture of superconductivity, both doublets are unoccupied in the ground state  $|g\rangle$  of the Josephson nanowire. However, superconducting circuits usually exhibit an excess population of quasiparticles that inhabit the continuum of states above the superconducting gap<sup>28</sup>. If one such quasiparticle becomes trapped in the sub-gap Andreev levels, its Hilbert space is spanned by the four energy eigenstates  $|s, n\rangle$ . Here,  $s = \uparrow, \downarrow$  denotes the quasiparticle spin with an arbitrary choice of spin label, and  $n = 1$  or  $2$  indicates the lower- or higher-energy doublet (Fig. 1a). At low temperatures (20 mK in this experiment), the quasiparticle will reside with high probability in the two spin states of the lower-energy doublet.

Detection of this spin with conventional cQED techniques necessitates lifting the spin degeneracy. As the Kramers theorem does not hold in the presence of a non-zero weak-link phase bias  $\varphi$ , the splitting of the spin states requires an additional ingredient. Here, this is provided by the spin-orbit interaction present in the multi-sub-band InAs nanowire; the interaction causes spin and translational degrees of freedom to hybridize and results in an energy-dependent spin texture<sup>29</sup>. (We continue to label these states as  $s = \uparrow, \downarrow$  for simplicity.) Critically, this interaction produces a spin-dependent Fermi velocity  $v_F^s$ , and therefore a spin-dependent propagation phase (as shown in Fig. 1b for positive momentum). The constructive interference condition that is required for Andreev levels to form is thereby modified and spin degeneracy is broken, as can be seen from the  $\varphi$  dispersion for levels deep in the gap:

$$\epsilon(\varphi, s) \simeq \pm \frac{\Delta \hbar v_F^s / \ell}{2(\Delta + \hbar v_F^s / \ell)} [(\varphi - \pi(2k + 1))] \quad (1)$$

where  $\pm$  corresponds to positive or negative current-carrying states and  $k$  is an integer. This relation can be viewed as a competition between two energy scales: the pair potential  $\Delta$  and the spin-dependent dwell energy  $\hbar v_F^s / \ell$ . Such a spin-split spectrum is shown in Fig. 1c with (grey lines, equation (1)) and without (coloured curves) normal scattering in the weak link included. This normal scattering will occur in all Josephson nanowires owing to disorder and intrinsic interface inhomogeneities or band curvature effects<sup>12,13,30</sup>. Although normal reflection also provides confinement, it is Andreev reflection that leads to the supercurrent that is crucial to this experiment.

Although a broken degeneracy is integral to our spin detection scheme, the higher energy doublet also plays a critical role. State readout of a quantum system by using cQED relies on the existence of microwave transitions between the system states  $|m\rangle$  to create a state-dependent dispersive shift  $\chi_m$  of a superconducting resonator's frequency. The extent to which each transition participates in  $\chi_m$  is determined by the coupling operator between the system and the resonator. Below, we demonstrate that the quasiparticle and the resonator are coupled through an approximately spin-conserving junction current operator  $J$ . As such, neither the direct spin-flipping intra-doublet transition nor the spin-flipping inter-doublet transition (thin arrows in Fig. 1c and thin curves in Fig. 1d) contributes appreciably to the dispersive shift. The dispersive shifts of the lower doublet states  $\chi_{s,1}$  are therefore dominated by the two remaining inter-doublet transitions (frequencies  $f_s$ ) (thick arrows in Fig. 1c and thick curves in Fig. 1d). Although these transitions are spin-conserving, the induced shift is nevertheless spin-dependent, which we describe by using second-order perturbation theory (see Supplementary Information Section 2):

$$\chi_{s,1} \simeq - \frac{\Phi_r^2}{2\pi \hbar^2} \frac{2f_s}{f_s^2 - f_r^2} |\langle s, 2 | J | s, 1 \rangle|^2 \quad (2)$$

Here,  $f_r = 9.188$  GHz is the bare resonator frequency and  $\Phi_r$  is the zero-point fluctuation of the resonator flux drop across the shared inductance (Fig. 1e). To detect such frequency shifts, we monitored the complex reflection amplitude  $\Gamma_{s,1}$  (real part  $I_{s,1}$ , imaginary part  $Q_{s,1}$ )  $I_{s,1} + iQ_{s,1}$  by using a microwave readout tone with frequency  $f_r$ . We found that  $\Gamma$  clustered into three distributions (Fig. 2b), which, as we now demonstrate, can be mapped to  $|g\rangle$ ,  $|\downarrow, 1\rangle$ , and  $|\uparrow, 1\rangle$  based on their dispersive shifts.

The dispersive shifts  $\chi_{s,1}$  and therefore the distribution centres  $\Gamma_{s,1}$  can be estimated from the  $\varphi$  dependence of the nanowire transition spectrum. We probed the spectrum by using two-tone spectroscopy (see Methods) as a function of an external flux  $\Phi$ , which set  $\varphi \simeq 2\pi \frac{\Phi}{\Phi_0} \text{mod}(2\pi)$ . We observed four transitions that we attribute to the inter-doublet transitions based on the qualitative agreement

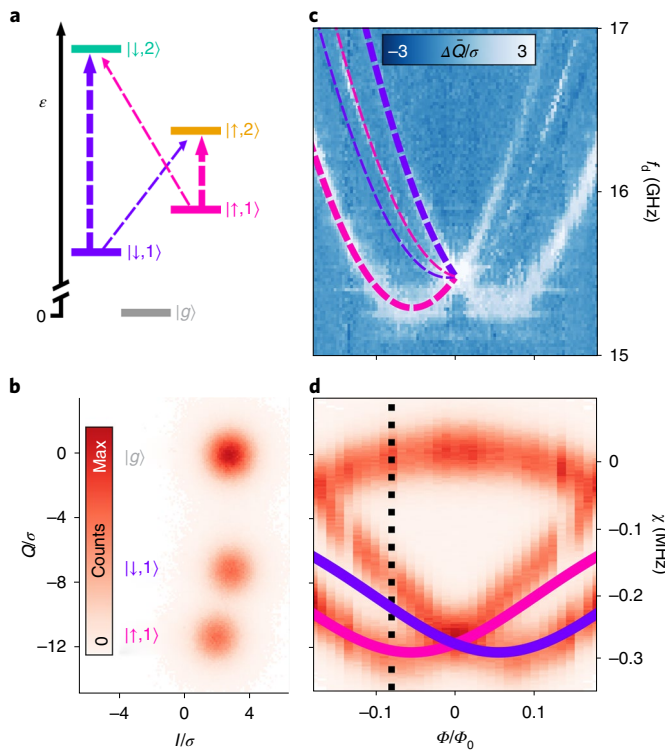


**Fig. 2 | Dispersive readout and spectroscopy of a trapped quasiparticle.** **a**, Level structure for  $\Phi < 0$ . As in Fig. 1c, transitions out of the lower doublet are shown by purple/pink dashed arrows, with thick/thin lines indicating whether the spin is maintained/flipped. **b**, Measured histogram of  $I/\sigma$ , where  $\sigma$  is the standard deviation of one distribution. The data cluster into three distributions that correspond to  $|g\rangle$ ,  $|\downarrow, 1\rangle$ , and  $|\uparrow, 1\rangle$ . **c**, Pulsed drive-probe spectroscopy of the nanowire reveals the four transitions shown in **a**, with fits to a simple model (see Supplementary Information Section 1) plotted for  $\Phi < 0$ . **d**, The distributions shown in **b** shift with  $\Phi$  as the detuning between the quasiparticle transitions and the resonator varies, from which the absolute dispersive shift (right axis) can be determined. The dashed line indicates  $\Phi$  for data in **b**, and coloured curves are predictions based on the extracted model parameters in **c** with only one additional free parameter (see main text), which captures the scale and shape of the behaviour.

of their  $\Phi$  dependence with that of the curves in Fig. 1d. We attribute the stark contrast in brightness to the coupling of the drive predominantly through the spin-conserving  $J$ . We fitted the spectrum with a simple model in which linearly dispersing Andreev levels of like spin undergo avoided crossings owing to normal scattering (see Supplementary Information Section 1). Around  $\Phi = 0$ , we extracted the slope of the  $|\downarrow, 1\rangle/|\uparrow, 1\rangle$  energy splitting and obtained  $d\Delta\epsilon/d\Phi = 1.8 \text{ nA}$ . Together with the device loop area of  $2,250 \mu\text{m}^2$  (see Methods), this yields a synthetic  $g$ -factor for the quasiparticle of approximately  $4 \times 10^5$  at low fields.

Our model of the nanowire spectrum clearly yields  $f_c(\Phi)$ , but it also facilitates insights into the matrix elements  $\langle s, 2|J|s, 1\rangle$  that are needed to calculate  $\chi_{s,1}$ , which is outlined here and detailed in Supplementary Information Section 2. From the fit, we infer a Hamiltonian  $H(\Phi)$  and therefore a current operator  $J(\Phi) = \frac{dH(\Phi)}{d\Phi}$  over the measured flux and frequency range. With  $\Phi_t$  as a free scaling parameter, we then calculate the  $\Phi$ -dependent  $\chi_{s,1}$  with equation (2) (Fig. 2d). We find a coupling strength of  $g_c \propto |\langle s, 2|J|s, 1\rangle|$  with maximum value  $g_c \approx 2\pi \times 35 \text{ MHz}$  at  $\Phi = \pm 0.08\Phi_0$  (see Extended Data Fig. 2). The qualitative agreement of the model with the measurement indicates that two of the distributions are associated with

the states  $|s, 1\rangle$ . Moreover, this agreement demonstrates that our crude model of a spin-conserving  $J$  describes the quasiparticle-resonator coupling in this regime. To understand the complete flux dependence of  $\chi_{s,1}$ , a more sophisticated model of  $J$  is necessary, such as an extension of ref. 12 to multiple doublets. The third distribution corresponds to  $|g\rangle$ ; all three states are visible simultaneously owing to the finite trapping lifetime of a quasiparticle in the Josephson nanowire, as discussed below.

We confirmed our interpretation of the state distributions and transition spectrum by directly measuring the population transfer that is induced by the microwave drive. As an example, we present the effect of driving with Gaussian pulses the two transitions available to a quasiparticle initially in  $|\uparrow, 1\rangle$  (pink dashed arrows in Fig. 3a,e). Two new distributions were revealed that are attributable to  $|\uparrow, 2\rangle$  and  $|\downarrow, 2\rangle$  (Fig. 3b,f). Because  $\chi_{s,2}$  was described approximately by equation (2) but with  $f_s \rightarrow -f_s$ , these distributions were located at positive  $Q$ . By varying the amplitude  $A$  of the  $|\uparrow, 1\rangle \leftrightarrow |\uparrow, 2\rangle$  pulse, we induced Rabi oscillations of the quasiparticle population between the two doublets (Fig. 3c). In contrast to coherent manipulation of quasiparticle pairs that has been demonstrated in the past<sup>7,8</sup>, our work features the coherent manipulation of an individual quasiparticle excitation of a superconductor.

Next, we inspected the relaxation dynamics of the trapped quasiparticle. Following a  $|\uparrow, 1\rangle$  to  $|\uparrow, 2\rangle$   $\pi$  pulse, we found that the quasiparticle decayed preferentially to  $|\uparrow, 1\rangle$  (Fig. 3d) on a timescale of  $\tau_{21,1} = 2.8 \pm 0.1 \mu\text{s}$ , whereas after a saturation pulse on the  $|\uparrow, 1\rangle \leftrightarrow |\downarrow, 2\rangle$  transition, the quasiparticle decayed preferentially to  $|\downarrow, 1\rangle$  on a timescale of  $\tau_{21,1} = 3.2 \pm 0.1 \mu\text{s}$  (short-time behaviour in Fig. 3g). We therefore observed that the spontaneous inter-doublet decay was spin-conserving, although we do not believe that it is limited by  $J$ -mediated Purcell decay (see Supplementary Information Section 3). Following the spin-flipping  $|\uparrow, 1\rangle \leftrightarrow |\downarrow, 2\rangle$  pulse, the initial spin-conserving relaxation resulted in an average spin polarization of the quasiparticle in the lower doublet, which then decayed on a timescale of  $\tau_s = 90 \pm 10 \mu\text{s}$  (Fig. 3g). We attributed the slight bi-exponential behaviour of  $|\downarrow, 1\rangle$  to spin relaxation within the upper doublet before decay to the lower doublet, and therefore fitted to only the long-time behaviour of  $|\downarrow, 1\rangle$  (see Methods for fit functions and further discussion). Such inter-doublet spin-flipping pulses followed by spin-conserving decay could therefore be used to initialize the spin state of a trapped quasiparticle, with a fidelity limited by the rate of  $|\uparrow, 1\rangle \rightarrow |\downarrow, 2\rangle$  population transfer compared to  $\tau_s$ .

The above results demonstrate that a trapped quasiparticle is a coherent object and resides with near-unity probability in the two low-energy spin states  $|\downarrow, 1\rangle$  and  $|\uparrow, 1\rangle$ , where its spin lifetime is more than an order of magnitude longer than the inter-doublet lifetime. To further characterize the spin lifetime and our spin detection fidelity, we then measured the undriven dynamics of the nanowire. We observed quantum jumps between these states by applying a continuous readout tone and partitioning the reflected signal into consecutive  $1.9 \mu\text{s}$  shots (Fig. 4b), with the state assigned based on the black dashed lines in Fig. 4a. We found a spin lifetime of  $\tau_s = 51 \pm 4 \mu\text{s}$  at this particular phase bias. In addition, we found a parity lifetime of  $31 \pm 1 \mu\text{s}$ , which is similar to that of previous reports<sup>7,8</sup>. Both spin flips and parity switches limited the fidelity of our spin readout. For perfect QND measurement, consecutive shots should always yield the same result, which means that transitions should never be observed. To compare to this ideal, we plot three separate histograms of  $Q$  based on the state assignment of the previous shot (Fig. 4c). We observed that consecutive shots yielded the same state  $|m\rangle$  with high probability  $p_{m,m}$ , with occasional transitions and mis-assignments that resulted in the peaks observed at the other distribution centres. We quantify these effects with the QND metric<sup>31</sup>  $\mathcal{F} = (p_{|\downarrow, 1\rangle, |\downarrow, 1\rangle} + p_{|\uparrow, 1\rangle, |\uparrow, 1\rangle})/2$ , which we find to be  $92.2 \pm 0.1\%$ .

Although a Zeeman effect was not necessary for our detection scheme, interaction with magnetic fields is a fundamental property

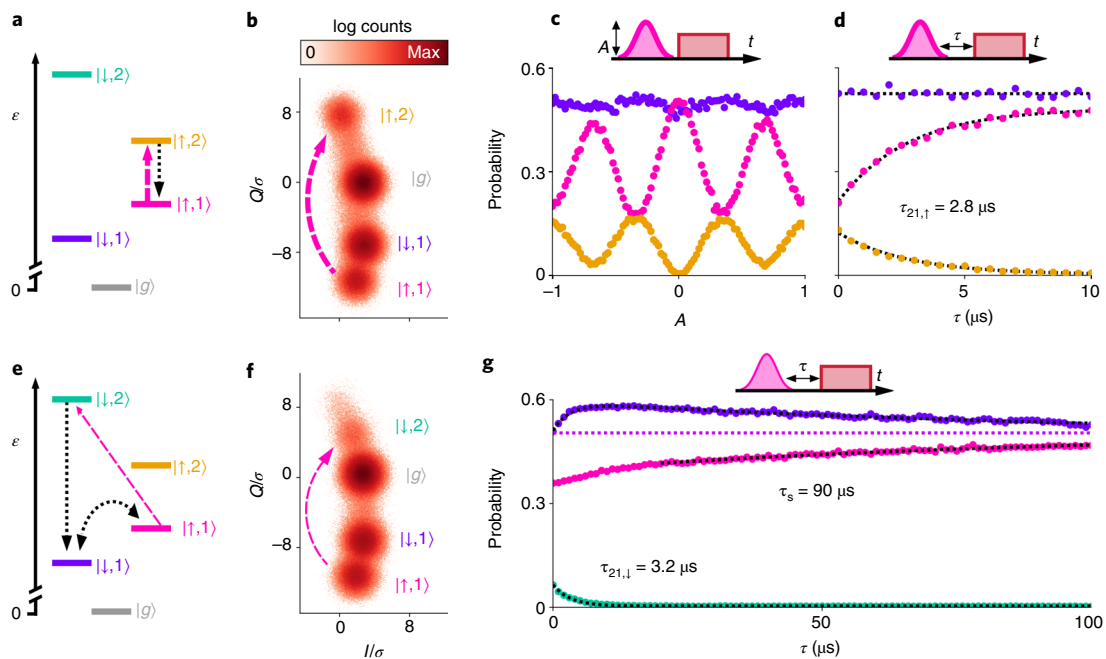


**Fig. 3 | Driven dynamics of a quasiparticle initially in  $|\uparrow, 1\rangle$  ( $\phi = 0.085\phi_0$ ).** **a–g.** The quasiparticle was excited into either  $|\uparrow, 2\rangle$  (**a–d**) or  $|\downarrow, 2\rangle$  (**e–g**) with Gaussian pulses on the transitions shown by the pink arrows in **a** and **e**. Following each pulse, the distributions that correspond to  $|\uparrow, 2\rangle/|\downarrow, 2\rangle$  were visible in the  $\Gamma$  histogram (**b** and **f**). In **c**, **d**, and **g**, we plot occupation probabilities for the states of interest as pulse sequence parameters are varied. Probabilities are computed as the number of counts within  $2\sigma$  of the distribution centres normalized by the steady-state counts. Fits to theory are denoted by dotted black curves (see Methods for fit functions). **c.** Varying the normalized amplitude  $A$  of the  $|\uparrow, 1\rangle \leftrightarrow |\uparrow, 2\rangle$  pulse resulted in coherent oscillations of the quasiparticle within the  $\uparrow$  manifold. **d.** Varying the delay  $\tau$  between the  $|\uparrow, 1\rangle \leftrightarrow |\uparrow, 2\rangle$  pulse and the readout pulse revealed exponential decay of the quasiparticle back to  $|\uparrow, 1\rangle$  with timescale  $\tau_{21,1}$  (black arrow in **a**). **g.** Following a  $|\uparrow, 1\rangle \leftrightarrow |\downarrow, 2\rangle$  pulse, an initial exponential decay to  $|\downarrow, 1\rangle$  with timescale  $\tau_{21,1}$  (single-headed black arrow in **e**) resulted in equal and opposite deviation of the  $|\downarrow, 1\rangle$  and  $|\uparrow, 1\rangle$  populations from their equilibrium value (pink dotted line). This spin polarization then decayed exponentially with timescale  $\tau_s$  (double-headed black arrow in **e**).

of spins. We determined the spin lifetime  $\tau_s$  as a function of both  $\varphi \simeq 2\pi \frac{\Phi}{\Phi_0} \bmod(2\pi)$  and a magnetic field  $B_\perp$  that was applied perpendicular to the chip substrate (Fig. 4d) by using a hidden Markov model algorithm (see Methods). At  $B_\perp = 0 \mu\text{T}$ , we observed that  $\tau_s$  increased with  $|\varphi|$  symmetrically about  $\varphi = 0$ . Note that, at  $\varphi/2\pi = 0.085$ ,  $\tau_s = 42 \pm 2 \mu\text{s}$ , which is shorter than the  $90 \pm 10 \mu\text{s}$  value obtained in the free-decay measurement (Fig. 3g), perhaps due to drive-induced saturation of the environment. The dependence of  $\tau_s$  on  $\varphi$  is correlated with the energy splitting between  $|\downarrow, 1\rangle$  and  $|\uparrow, 1\rangle$ , which reaches zero at  $\varphi = 0$  (Fig. 1d). Application of a positive (negative)  $B_\perp$  resulted in a positive (negative) shift of the  $\varphi$  dependence. This can be explained by a Zeeman-like shift of the Andreev levels, which is consistent with the observed spectrum at  $B_\perp = 380 \mu\text{T}$  (see Extended Data Fig. 7) and is expected for a magnetic field that is applied parallel to the spin-orbit field<sup>11,13</sup>.

The source of quasiparticle spin flips is currently unknown. Electron spin flips in semiconductor quantum dots are typically caused by some combination of hyperfine interactions, spin-orbit coupling, and phonon emission<sup>1</sup>. Away from  $\Delta\epsilon = 0$ , direct electron–nuclei ‘flip-flops’ quickly become suppressed because of the small nuclear spin energy scale. As  $\Delta\epsilon$  is increased further,  $\tau_s$  typically decreases owing to, among other factors, an increasing phonon density of states. This trend is opposite to our observation, although we note that for this experiment the phonons may be quasi-one-dimensional for the investigated spin energies  $\Delta\epsilon < 600 \text{ MHz}$  owing to transverse confinement. An additional clue is that increasing the temperature did not affect  $\tau_s$  until approximately  $150 \text{ mK}$  (see Extended Data Fig. 8). Further theoretical and experimental work is necessary to understand the source of quasiparticle spin flips in Josephson nanowires.

In summary, we have demonstrated that the spin of an individual quasiparticle that is trapped in a Josephson nanowire can be detected by coupling the delocalized spin-dependent supercurrent to a superconducting resonator, and that the quasiparticle can be manipulated coherently. We attempted to drive the spin-flipping intra-doublet transition directly, but were unable to do so. The realization of cQED-integrated superconducting spin qubits<sup>9,10,12</sup> requires full coherent control over the quasiparticle spin. This could be achieved through Raman transitions through the higher energy doublet or by applying a magnetic field (on the order of  $10\text{--}100 \text{ mT}$ ) to enable direct,  $J$ -induced intra-doublet microwave driving<sup>12,13</sup>. Furthermore, for larger fields (on the order of  $1 \text{ T}$ ) the nanowire could be tuned to a topological phase<sup>14,15</sup> in which the techniques presented here would reveal the quasiparticle dynamics of the Majorana mode of the weak link. As quasiparticle trapping lifetimes will limit both Majorana-based topological qubits and superconducting spin qubits, application of our measurement scheme to such superconductor–semiconductor heterostructures could provide the detailed understanding of quasiparticle dynamics that is essential for future progress.

### Online content

Methods, additional references, Nature Research reporting summaries, source data, extended data, supplementary information, acknowledgements, peer review information, details of author contributions and competing interests, and statements of data and code availability are available at <https://doi.org/10.1038/s41567-020-0952-3>.

Received: 28 August 2019; Accepted: 1 June 2020;  
Published online: 06 July 2020

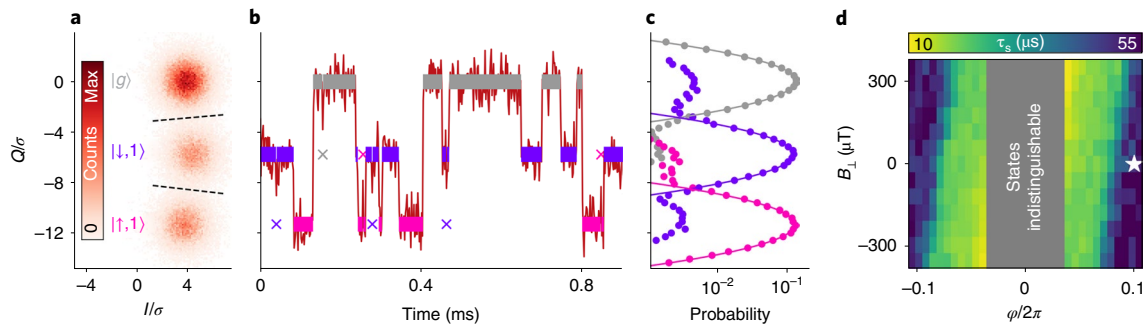


**Fig. 4 | Quantum non-demolition readout of the quasiparticle spin ( $\Phi = 0.100\Phi_0$ ).** **a**, The system state was assigned to be  $|g\rangle$ ,  $|\downarrow, 1\rangle$ , or  $|\uparrow, 1\rangle$  based on thresholds indicated by the black dashed lines. **b**,  $Q(t)$  reveals quantum jumps between the three states. Coloured bars indicate state assignments, with isolated points indicated by crosses and coloured by the most likely state. **c**, Histograms of  $Q$  separated by the state assignment of the previous measurement (indicated by colour). Solid lines are Gaussian fits. **d**, By analysing  $I(t)$  with a hidden Markov model (see Methods), the spin lifetime  $\tau_s$  was determined as a function of both  $\varphi$  and a magnetic field  $B_{\perp}$  applied perpendicular to the chip substrate. The star indicates the bias for data in **a**, **b**, and **c**.

## References

- Hanson, R., Kouwenhoven, L. P., Petta, J. R., Tarucha, S. & Vandersypen, L. M. K. Spins in few-electron quantum dots. *Rev. Mod. Phys.* **79**, 1217–1265 (2007).
- Nakajima, T. et al. Quantum non-demolition measurement of an electron spin qubit. *Nat. Nanotechnol.* **14**, 555–560 (2019).
- Beenakker, C. W. J. & van Houten, H. Josephson current through a superconducting quantum point contact shorter than the coherence length. *Phys. Rev. Lett.* **66**, 3056–3059 (1991).
- Furusaki, A. & Tsukada, M. Current-carrying states in Josephson junctions. *Phys. Rev. B* **43**, 10164–10169 (1991).
- Blais, A., Huang, R.-S., Wallraff, A., Girvin, S. M. & Schoelkopf, R. J. Cavity quantum electrodynamics for superconducting electrical circuits: an architecture for quantum computation. *Phys. Rev. A* **69**, 062320 (2004).
- Wallraff, A. et al. Strong coupling of a single photon to a superconducting qubit using circuit quantum electrodynamics. *Nature* **431**, 162–167 (2004).
- Janvier, C. et al. Coherent manipulation of Andreev states in superconducting atomic contacts. *Science* **349**, 1199–1202 (2015).
- Hays, M. et al. Direct microwave measurement of Andreev-bound-state dynamics in a semiconductor-nanowire Josephson junction. *Phys. Rev. Lett.* **121**, 047001 (2018).
- Chitchev, N. M. & Nazarov, Y. V. Andreev quantum dots for spin manipulation. *Phys. Rev. Lett.* **90**, 226806 (2003).
- Padurariu, C. & Nazarov, Y. V. Theoretical proposal for superconducting spin qubits. *Phys. Rev. B* **81**, 144519 (2010).
- Reynoso, A. A., Usaj, G., Balseiro, C. A., Feinberg, D. & Avignon, M. Spin-orbit induced chirality of Andreev states in Josephson junctions. *Phys. Rev. B* **86**, 214519 (2012).
- Park, S. & Yeyati, A. L. Andreev spin qubits in multichannel Rashba nanowires. *Phys. Rev. B* **96**, 125416 (2017).
- Tosi, L. et al. Spin-orbit splitting of Andreev states revealed by microwave spectroscopy. *Phys. Rev. X* **9**, 011010 (2019).
- Fu, L. & Kane, C. L. Superconducting proximity effect and Majorana fermions at the surface of a topological insulator. *Phys. Rev. Lett.* **100**, 096407 (2008).
- Mourik, V. et al. Signatures of Majorana fermions in hybrid superconductor-semiconductor nanowire devices. *Science* **336**, 1003–1007 (2012).
- Roy, A. & Devoret, M. Introduction to parametric amplification of quantum signals with Josephson circuits. *C. R. Phys.* **17**, 740–755 (2016).
- Petersson, K. D. et al. Circuit quantum electrodynamics with a spin qubit. *Nature* **490**, 380–383 (2012).
- Samkharadze, N. et al. Strong spin-photon coupling in silicon. *Science* **359**, 1123–1127 (2018).
- Mi, X. et al. A coherent spin-photon interface in silicon. *Nature* **555**, 599–603 (2018).
- Harvey, S. P. et al. Coupling two spin qubits with a high-impedance resonator. *Phys. Rev. B* **97**, 235409 (2018).
- Landig, A. J. et al. Coherent spin-photon coupling using a resonant exchange qubit. *Nature* **560**, 179–184 (2018).
- Cubaynes, T. et al. Highly coherent spin states in carbon nanotubes coupled to cavity photons. *npj Quantum Inf.* **5**, 47 (2019).
- Borjans, F., Croot, X. G., Mi, X., Gullans, M. J. & Petta, J. R. Resonant microwave-mediated interactions between distant electron spins. *Nature* **577**, 195–198 (2020).
- Zheng, G. et al. Rapid gate-based spin read-out in silicon using an on-chip resonator. *Nat. Nanotechnol.* **14**, 742–746 (2019).
- West, A. et al. Gate-based single-shot readout of spins in silicon. *Nat. Nanotechnol.* **14**, 437–441 (2019).
- Urdampilleta, M. et al. Gate-based high fidelity spin readout in a CMOS device. *Nat. Nanotechnol.* **14**, 737–741 (2019).
- van Woerkom, D. J. et al. Microwave spectroscopy of spinful Andreev bound states in ballistic semiconductor Josephson junctions. *Nat. Phys.* **13**, 876–881 (2017).
- Aumentado, J., Keller, M. W., Martinis, J. M. & Devoret, M. H. Nonequilibrium quasiparticles and  $2e$  periodicity in single-Cooper-pair transistors. *Phys. Rev. Lett.* **92**, 066802 (2004).
- Governale, M. & Zülicke, U. Spin accumulation in quantum wires with strong Rashba spin-orbit coupling. *Phys. Rev. B* **66**, 073311 (2002).
- Sriram, P., Kalantre, S. S., Gharavi, K., Baugh, J. & Muralidharan, B. Supercurrent interference in semiconductor nanowire Josephson junctions. *Phys. Rev. B* **100**, 155431 (2019).
- Touzard, S. et al. Gated conditional displacement readout of superconducting qubits. *Phys. Rev. Lett.* **122**, 080502 (2019).

**Publisher's note** Springer Nature remains neutral with regard to jurisdictional claims in published maps and institutional affiliations.

© The Author(s), under exclusive licence to Springer Nature Limited 2020

## Methods

**Experimental device and setup.** The experimental device was fabricated on a sapphire substrate. (Fig. 1c shows a micrograph of a similar  $\ell = 500$  nm device, as our device was inaccessible owing to ongoing measurements; further device images are provided in Extended Data Fig. 1 with a full schematic of the cryogenic setup.) After performing microwave simulations of the circuit by using Sonnet Suites 16, we patterned the readout resonator and control structures by electron-beam lithography and reactive-ion etching of sputtered niobium titanium nitride (NbTiN). The NbTiN film had a thickness of 150 nm and a sheet kinetic inductance of 0.6 pH per square, which we took into account when calculating the shared inductance between the nanowire and the resonator. An InAs nanowire was grown on [001] wurtzite by using molecular beam epitaxy with epitaxial Al that coated two of six facets, and was then deposited by using a micromanipulator. The weak link was defined by selectively wet-etching a 500 nm long section of the Al shell, and was contacted to the rest of the circuit by using NbTiN. After connecting the device to external circuitry (Extended Data Fig. 1), we cooled the device in a dilution refrigerator with a base temperature of 20 mK. We used a coil external to the device to apply a magnetic field approximately perpendicular to the device substrate; this coil generated the flux  $\Phi$ . The data displayed in Figs. 2, 3, 4a–c were obtained at  $|\Phi/\Phi_0| < 1$ , and as such we interpreted the flux as a phase bias  $\varphi \approx 2\pi\Phi/\Phi_0$ . The data displayed in Fig. 4d were obtained with the same coil, but  $\Phi$  was swept over approximately 1,000  $\Phi_0$ . For this measurement, we therefore interpreted  $\Phi$  as both a phase bias  $\varphi \approx 2\pi\frac{\Phi}{\Phi_0} \bmod(2\pi)$  and a magnetic field  $B_{\perp} = \Phi/A_{\text{loop}}$ .

**Measurement.** We performed microwave reflectometry of the resonator by using a readout tone at the bare resonator frequency of 9.188 GHz, which produced an average of approximately 10 photons in the resonator during measurement. After interacting with the device (Fig. 1c), the readout tone was routed through an amplification chain that consisted of a SNAIL parametric amplifier (SPA)<sup>32</sup> at base temperature, a high-electron-mobility transistor (HEMT) amplifier at 4 K, and finally room-temperature amplifiers (Extended Data Fig. 1). The signal was then down-converted to 50 MHz before it was fed into a data acquisition card. The reflection amplitude  $\Gamma$  was computed by comparing this 50 MHz signal to a 50 MHz reference and integrating for 1.9  $\mu\text{s}$ .

At low gate voltages ( $V_g < -2$  V), we observed no dependence of  $\Gamma$  on the current through our  $\Phi$ -bias coil. As we increased  $V_g$ , we observed ranges of  $V_g$  in which  $\Gamma$  depended strongly on  $\Phi$ . We attribute this to the transparency of the nanowire conductance channels that fluctuated close to unity<sup>3,27,33</sup>. To locate the transitions that caused these shifts, we performed pulsed drive-probe spectroscopy (2.5  $\mu\text{s}$  drive pulse, 1.9  $\mu\text{s}$  readout pulse). In the vicinity of  $V_g = -1.36$  V, we observed the transitions that are discussed in the main text (Fig. 2c). To minimize electric-field-induced decoherence, we made fine adjustments to  $V_g$  such that at  $\Phi = 0$  the transitions were at a local maximum in  $V_g$  (Extended Data Fig. 4). In addition to  $V_g$ , we used two additional gates on the proximitized<sup>34</sup> sections of the nanowire to gain additional electrostatic control (Extended Data Fig. 1). Both gates were biased to the same nanowire (nw) voltage  $V_{\text{nw}} = 0.9$  V for all presented data.

**Two-tone spectroscopy.** In Fig. 2c, we show the result of a two-tone spectroscopy measurement in which a square drive pulse is first applied (carrier frequency  $f_{\text{d}}$ , pulse length 1  $\mu\text{s}$ ) before the system state is measured by using a readout pulse. When the drive tone was resonant with a transition, population was transferred between the Andreev levels, which we detected by measuring shifts in the averaged reflection coefficient  $\Gamma$ .

**Definition of synthetic  $g$ -factor.** Here, we define the  $g$ -factor by using the slope of the linear energy splitting between the two spin states under the application of magnetic field:  $g = \frac{1}{\mu_B} \frac{d\Delta_C}{dB_{\perp}}|_{B_{\perp}=0} = \frac{A_{\text{loop}}}{\mu_B} \frac{d\Delta_C}{d\Phi}|_{\Phi=0}$ . We call this  $g$ -factor ‘synthetic’ because it depends on the circuit geometry.

**Analysis of driven dynamics.** The Gaussian pulses used in the experiments that are shown in Fig. 3b–d had standard deviations of 20 ns, whereas the pulses used in the experiments shown in Fig. 3fg had standard deviations of 250 ns owing to the greater total energy required to induce spin-flipping transitions. To compute the probabilities plotted in Fig. 3c,d,g, we first counted the number of shots within  $2\sigma$  of the distribution centres. Shots outside of these regions were left unassigned. Extended Data Fig. 6 illustrates this for the measurement shown in Fig. 3c and includes counts assigned to the  $|g\rangle$  population as well as unassigned counts. For Fig. 3c,d,g, we then normalized by the steady-state (undriven) counts for the primary states of interest ( $|\downarrow, 1\rangle$ ,  $|\uparrow, 1\rangle$ , and  $|\uparrow, 2\rangle$ ) for the Fig. 3c measurement). Owing to decay from  $|\uparrow, 2\rangle$  to  $|\uparrow, 1\rangle$  during measurement, some shots were assigned mistakenly to  $|g\rangle$  and  $|\downarrow, 1\rangle$  or were unassigned because their mid-flight capture resulted in a value of  $\Gamma$  that was not associated with any one state distribution. This resulted in small oscillations in the apparent populations of these states, large oscillations of the number of shots not assigned to any state (Extended Data Fig. 6), and also what appears to be an unequal probability change between states  $|\uparrow, 2\rangle$  and  $|\uparrow, 1\rangle$  in Fig. 3c. The magnitude of these unintended oscillations decreased with shorter integration time, which is consistent with our interpretation; however,

the discrimination power also suffered. Such decay during measurement also explains the  $|\downarrow, 2\rangle$  population observed in Fig. 3f, as well as the unequal population deviations at  $\tau = 0$  observed in Fig. 3d,g.

A simultaneous fit of the form  $P_{\downarrow,1} = c_{\downarrow,1}$ ,  $P_{\uparrow,1} = -A_{\downarrow,1}e^{-\tau/\tau_{\downarrow,1}} + c_{\downarrow,1}$ , or  $P_{\downarrow,2} = A_{\downarrow,2}e^{-\tau/\tau_{\downarrow,2}} + c_{\downarrow,2}$  was applied to the three curves of Fig. 3d. Because the data were not normalized, the only parameter shared between the three curves was  $\tau_{\downarrow,1}$ . Similarly, the three curves of Fig. 3d were fitted simultaneously with  $P_{\downarrow,1} = -A_{\downarrow,21}e^{-\tau/\tau_{\downarrow,21}} + A_{\downarrow,1}e^{-\tau/\tau_{\downarrow,1}} + c_{\downarrow,1}$ ,  $P_{\uparrow,1} = -A_{\uparrow,2}e^{-\tau/\tau_{\uparrow,2}} + c_{\uparrow,1}$ , or  $P_{\downarrow,2} = A_{\downarrow,2}e^{-\tau/\tau_{\downarrow,2}}$ . Here, the shared parameters were  $\tau_{\downarrow,1}$  and  $\tau_{\uparrow,1}$ . As discussed in the main text, we fitted to only the  $|\uparrow, 1\rangle$  data for times of greater than 20  $\mu\text{s}$  owing to the observed bi-exponential decay. We attribute this to spin mixing within the upper doublet before decay to the lower doublet. However, we were unable to measure these dynamics accurately owing to the large overlap between the  $|\uparrow, 2\rangle$  and  $|\downarrow, 2\rangle$  distributions and the relative weakness of the effect (the quasiparticle decays to the lower doublet before much spin mixing can occur).

**Quantum jump analysis.** We first tuned the flux bias to  $\Phi = 0.100\Phi_0$  to maximize the separation of the  $|g\rangle$ ,  $|\downarrow, 1\rangle$ , and  $|\uparrow, 1\rangle$   $\Gamma$  distributions. The spin lifetime  $\tau_S$  and quasiparticle trapping lifetime were extracted from  $\Gamma(t)$  by using a hidden Markov model algorithm<sup>35,36</sup>. This analysis assumes that the system possesses three states ( $|g\rangle$ ,  $|\downarrow, 1\rangle$ , and  $|\uparrow, 1\rangle$ ), and that each state  $|m\rangle$  emits values of  $\Gamma$  with different (but potentially overlapping) probability distributions  $p(\Gamma|m)$ . Importantly,  $p(\Gamma|m)$  does not need to be known a priori. By analysing  $\Gamma(t)$ , the algorithm yields the most probable  $p(\Gamma|m)$ , state assignments at each  $t$ , and transition rates  $\gamma_{n,m}$  from  $|m\rangle$  to  $|n\rangle$ . We measured all six  $\gamma_{n,m}$  as a function of  $\varphi$ ,  $B_{\perp}$ , and the temperature of the mixing chamber (Extended Data Figs. 6, 8 and Supplementary Information Section 4). The spin lifetime was computed as  $\tau_S = 1/(\gamma_{\downarrow,1} + \gamma_{\uparrow,1})$ , and the trapping lifetime was computed as  $1/(\gamma_{0,\downarrow} + \gamma_{0,\uparrow})$ . Here, we distinguish between the trapping lifetime and the parity lifetime  $1/(\gamma_{\downarrow,0} + \gamma_{\uparrow,0} + \gamma_{0,\downarrow} + \gamma_{0,\uparrow}) = 21 \pm 1 \mu\text{s}$ , because it is the trapping lifetime that limits the fidelity of the spin detection.

## Data availability

Source data are provided with this paper. All other data that support the plots within this paper and other findings of this study are available from the corresponding author upon reasonable request.

## References

- Frattini, N. E., Sivak, V. V., Lingenfelter, A., Shankar, S. & Devoret, M. H. Optimizing the nonlinearity and dissipation of a SNAIL parametric amplifier for dynamic range. *Phys. Rev. Appl.* **10**, 054020 (2018).
- Goffman, M. F. et al. Conduction channels of an InAs-Al nanowire Josephson weak link. *New J. Phys.* **19**, 092002 (2017).
- Chang, W. et al. Hard gap in epitaxial semiconductor–superconductor nanowires. *Nat. Nanotechnol.* **10**, 232–236 (2015).
- Press, W. H., Teukolsky, S. A., Vetterling, W. T. & Flannery, B. P. *Numerical Recipes in C++: The Art of Scientific Computing* 2nd edn (Cambridge Univ. Press, 2002)..

## Acknowledgements

We thank N. Frattini and V. Sivak for providing the SNAIL parametric amplifier. We are grateful to M. Goffman, H. Pothier, L. Tosi, and C. Urbina for sharing their experimental results and thoughts. We thank J. Moreno and A. L. Yeyati for important discussions on the inter-doublet decay dynamics. We are grateful to S. Frolov, L. Frunzio, L. Glazman, M. Houzet, C. Marcus, S. Shankar, and S. Touzard for useful discussions. This research was supported by the US Office of Naval Research (N00014-16-1-2270) and by the US Army Research Office (W911NF-18-1-0020, W911NF-18-1-0212 and W911NF-16-1-0349). J.N. acknowledges support from the Danish National Research Foundation. G.d.L. acknowledges support from the European Union’s Horizon 2020 research and innovation programme under Marie Skłodowska–Curie grant agreement no. 656129. D.B. acknowledges support from the Netherlands Organisation for Scientific Research (NWO) and Microsoft Corporation Station Q. A.G. and J.N. acknowledge support from the Horizon 2020 research and innovation programme of the European Union: A.G. received funding from European Research Council grant no. 804988 (SiMS), and A.G. and J.N. received support from European Research Council grant no. 828948 (AndQC) and QuantERA project no. 127900 (SuperTOP).

## Author contributions

M.H., K.S., D.B., G.d.L., A.G., and M.H.D. designed the experimental setup. P.K. and J.N. developed the nanowire materials. D.B. and A.G. fabricated the device. M.H. and V.F. performed the measurements and developed physical models. M.H., V.F., K.S., S.D., and M.H.D. analysed the data. M.H., V.F., and M.H.D. wrote the manuscript with feedback from all authors.

## Competing interests

The authors declare no competing interests.

**Additional information**

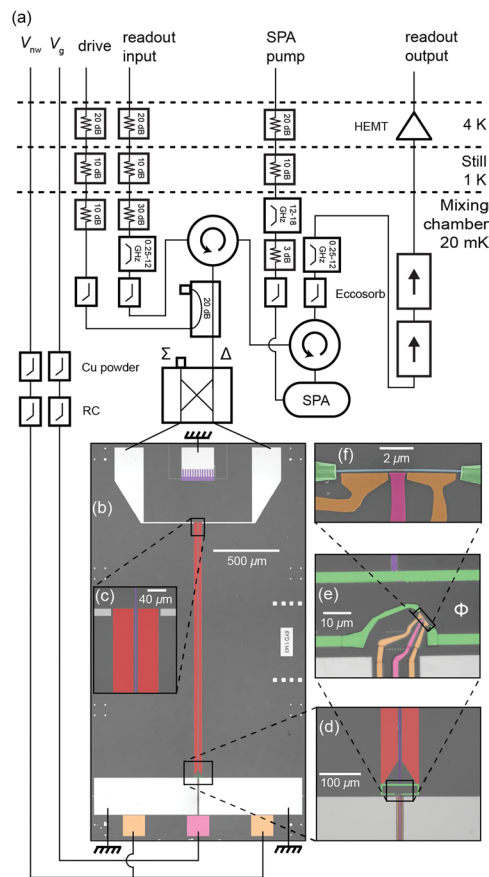
**Extended data** is available for this paper at <https://doi.org/10.1038/s41567-020-0952-3>.

**Supplementary information** is available for this paper at <https://doi.org/10.1038/s41567-020-0952-3>.

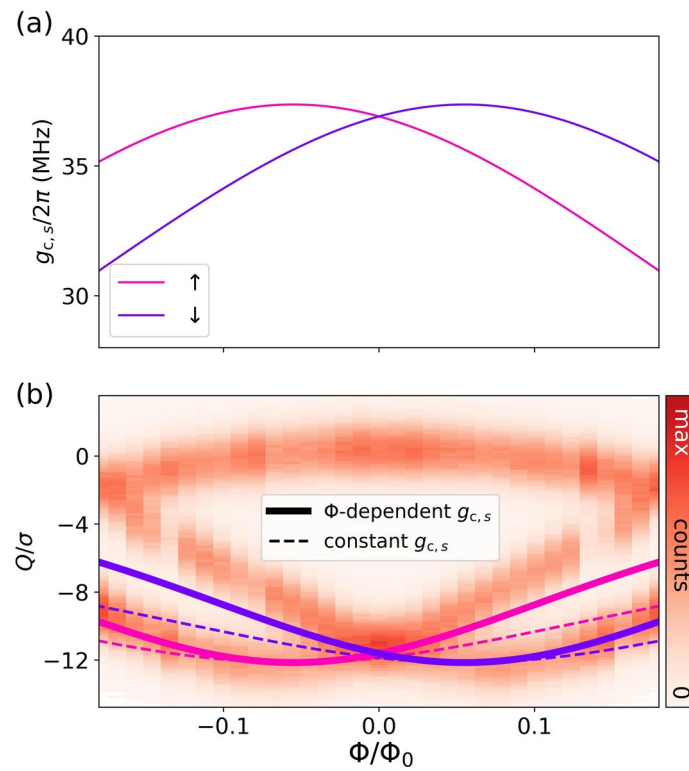
**Correspondence and requests for materials** should be addressed to M.H., V.F. or M.H.D.

**Peer review information** *Nature Physics* thanks W. Belzig, X. Mi, and the other, anonymous, reviewer(s) for their contribution to the peer review of this work.

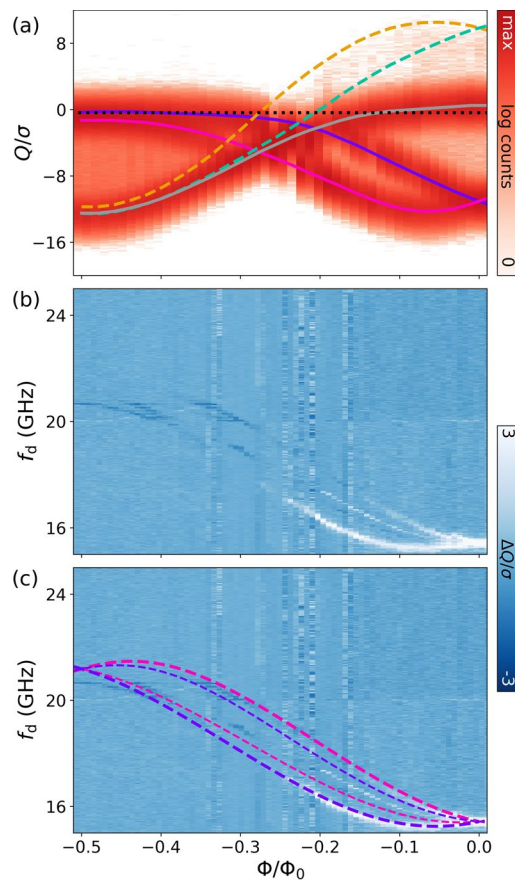
**Reprints and permissions information** is available at [www.nature.com/reprints](http://www.nature.com/reprints).



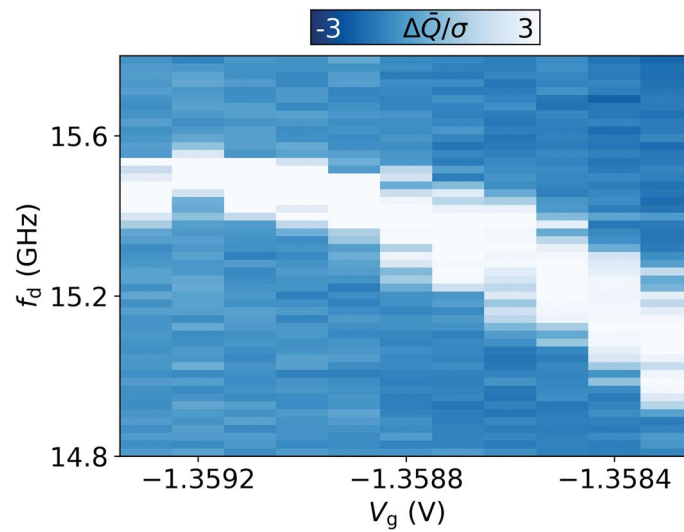
**Extended Data Fig. 1 | Cryogenic wiring diagram and device micrographs.** Optical micrograph **e**, is of the device on which the presented measurements were performed. Optical micrographs **b**, **c**, **d**, and scanning electron micrograph **f**, are of an extremely similar (unmeasured) device, the main difference being that the length of the weak link is 750nm instead of 500nm. The microwave readout and drive tones pass through the depicted circuitry **a**, before being routed through the  $\Delta$  port of a  $180^\circ$  hybrid resulting in differential microwave voltages at the device input. After reaching two coupling capacitors (**c**), the readout tone was reflected off the differential  $\lambda/4$  mode of the coplanar strip resonator (red, frequency  $f_r = 9.18843\text{GHz}$ , coupling  $\kappa_c = 2\pi \times 1.23\text{MHz}$ , internal loss  $\kappa_i = 2\pi \times 1.00\text{MHz}$ ) and then routed through the depicted amplification chain (**a**), which was comprised of a SNAIL parametric amplifier (SPA), HEMT, and room-temperature amplifiers. In this circuit, the drive tone creates an ac phase drop across the nanowire (**f**), which is embedded in the superconducting  $\Phi$ -bias loop (green) at the end of the resonator (**d,e**). One edge of the loop connects the two strips of the resonator and thereby forms the shared inductance with the nanowire. We controlled the electrostatic potential in the nanowire weak link (**f**) with a dc gate (pink, voltage  $V_g$ ). Gates on the nanowire leads (orange) were used to gain additional electrostatic control, which were biased to the same voltage  $V_{nw} = 0.9\text{V}$  for all presented data. To reference the resonator/nanowire island to ground, an additional strip runs between the resonator strips, and connects to a large finger capacitor (purple). This strip does not significantly perturb the resonator's microwave properties because it resides at the zero voltage point with respect to the resonator's differential mode.



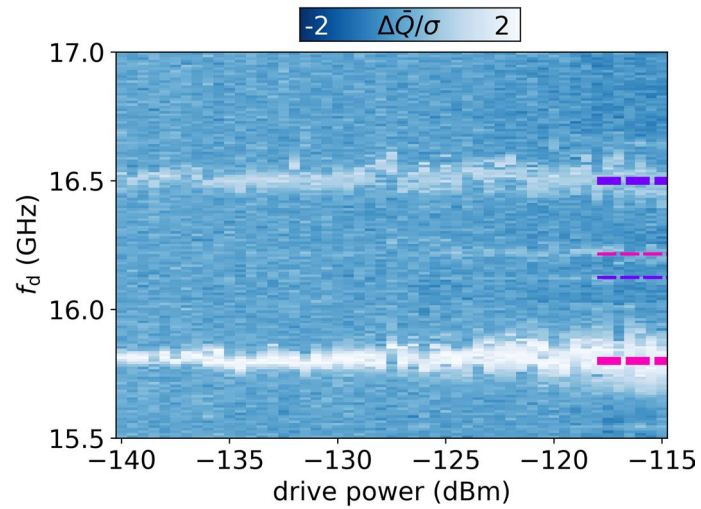
**Extended Data Fig. 2 |  $\Phi$ -dependence of  $g_{c,s}$ .** **a**, Extracted coupling strengths  $g_{c,s}$  for the two inter-doublet spin conserving transitions. The peaks coincide with the minimum frequency of the transitions ( $\Phi = \pm \Phi_{\text{cross}}$ ) because this is where the mixing between current and energy eigenstates is strongest (see Supplementary Information Section 1). **b**, Same data as shown in Fig. 2(d). Solid lines are the predicted  $\chi_{s,1}$  as in the main text, and dashed lines are the  $\chi_{s,1}$  if  $g_{c,s}$  is assumed to be constant at its maximum value.



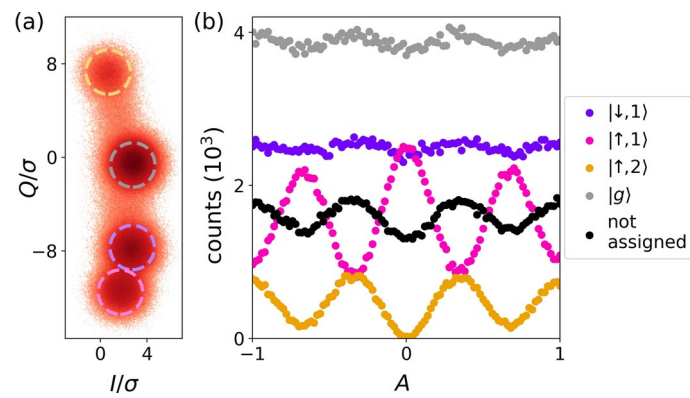
**Extended Data Fig. 3 | Full  $\Phi$ -dependence of spectrum and dispersive shifts.** **a**,  $\Phi$ -dependence of  $Q$  over a full half flux quantum. The  $|\downarrow, 1\rangle$  and  $|\uparrow, 1\rangle$  distributions (traced with purple and pink splines respectively) remain below the bare resonator  $Q$  (black dotted line) over the full  $\Phi$  range, indicating negative dispersive shifts which are inconsistent with  $\chi$  resulting from coupling to the inverse inductance operator. The dispersive shift of  $|g\rangle$  (traced with the gray spline) is likely due to a pair transition with frequency above our measurement bandwidth. We also observe a small number of counts around  $\Phi=0$  at positive  $Q$ , indicating a residual quasiparticle population in  $|\uparrow, 2\rangle$  and  $|\downarrow, 2\rangle$ . Assuming the observed dispersive shift of  $|g\rangle$  is due only to the properties of the lower doublet, the dispersive shift of a quasiparticle in the upper doublet should be given by  $\chi_{s,2} = -\chi_{s,1} + \chi_0$ . Based on this formula and the plotted splines, we estimated the  $\Phi$ -dependence of the  $|\downarrow, 2\rangle$  and  $|\uparrow, 2\rangle$  distributions (dashed, teal, and yellow). The predictions track roughly with the residual counts in the vicinity of  $\Phi=0$  before crossing the bare resonator  $Q$ . **(b)** Spectroscopy over the same flux range. The inter-doublet transitions have maximum frequency at  $\Phi = -0.5\Phi_0$ , consistent with Fig. 1(d). We attribute the sign change in the measured  $\Delta\bar{Q}$  to the crossings of  $\chi_{s,1}$  with  $\chi_{s,2}$  indicated in **(a)**. **(c)** Attempted modeling of the transitions using the double-barrier model of Ref. <sup>13</sup>. Here we extract a chemical potential (as measured from the bottom of a sub-band) of 0.65 meV and a Rashba coefficient of 43 meV\*nm. The effective transparencies of the two barriers are  $t_1=0.32$  and  $t_2=0.46$ .



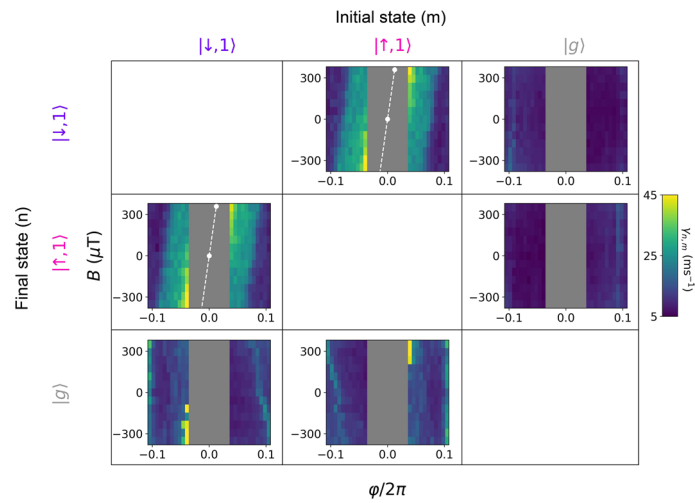
**Extended Data Fig. 4 | Spectroscopy of the inter-doublet transitions at the  $\Phi = 0$  degeneracy point while  $V_g$  is varied.** The transition frequency changes due to mesoscopic conductance fluctuations<sup>8,27,33</sup>, and a local maximum is observed around  $V_g = -1.3592$  V. The linewidth is visibly narrower at this local maximum, indicating that electric field noise is the dominant source of dephasing. To minimize this dephasing, we performed the measurements presented in the main text at  $V_g = -1.3592$  V.



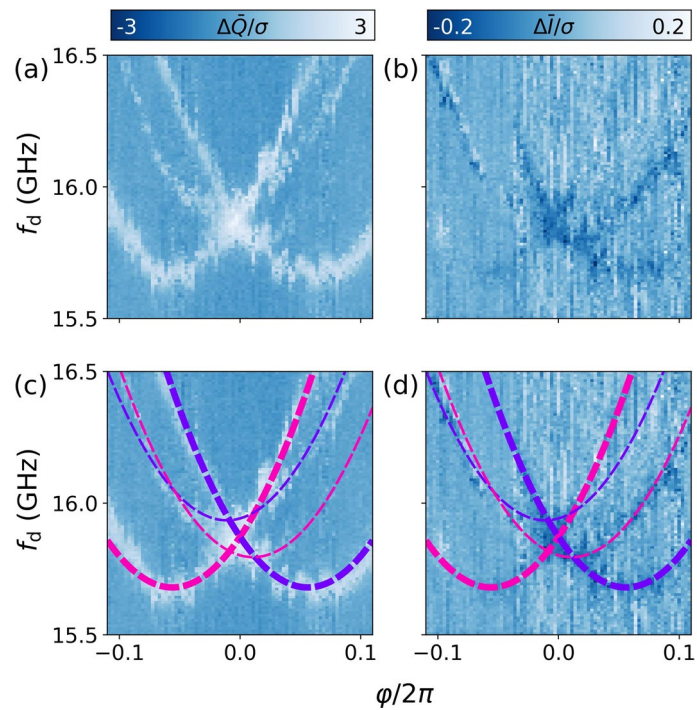
**Extended Data Fig. 5 | Brightness of the four inter-doublet transitions as a function of estimated drive power at the device.** At low powers, only the spin-conserving transitions are visible, but as the power is increased the spin-flipping transitions also appear. Note that the spin-flipping transitions at the maximum power (-115 dBm) are still substantially dimmer than the spin-preserving transitions at the lowest power (-140 dBm).



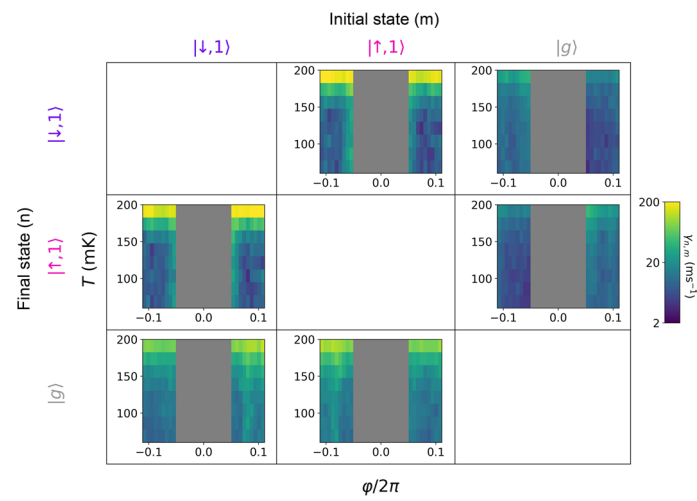
**Extended Data Fig. 6 | Further detail for the analysis of the Rabi experiment depicted in Fig. 3(d).** **a**, Histogram of all measurement shots taken during the experiment. Shots inside the dashed circles (radius  $2\sigma$ ) were assigned to the corresponding state. Shots outside these regions were left unassigned. Note that here we also include  $|g\rangle$  for illustration. **b**, At each value of the normalized pulse amplitude  $A$ , we count the number of points inside each of the four depicted circles in (a). The number of unassigned counts is also plotted. See Methods for further details and comments.



**Extended Data Fig. 7 |** The six extracted transition rates  $\gamma_{n,m}$  between  $|g\rangle$ ,  $|\downarrow, 1\rangle$ , and  $|\uparrow, 1\rangle$  as a function of  $\varphi$  and  $B_{\perp}$  at the base temperature of the fridge  $T = 20\text{mK}$ . White data points on the spin-flipping rate plots indicate the  $|\downarrow, 1\rangle/|\uparrow, 1\rangle$  degeneracy point at  $B_{\perp} = 0 \mu\text{T}$ ,  $380 \mu\text{T}$  (see Main Text Fig. 2(c), Extended Data Fig. 7, Supplementary Information Section 4). The dashed lines connect these points and are guides for the eye.



**Extended Data Fig. 8 | Spectroscopy at  $B_{\perp} = 380 \mu\text{T}$ .** Note that here there was a slight overall frequency shift due to a change in the electrostatic environment of the nanowire. Here we plot both  $I$  (**a**) and  $Q$  (**b**) to present information in both quadratures. The observed instabilities varied with time, and occurred when operating our flux coil at high current. The same data is plotted in (**c**)/(**d**), but with overlaid fits. We describe the data by the model used in Fig. 2(c), but we include an additional Zeeman-like term (see Supplementary Information Section 4).



**Extended Data Fig. 9** | The six extracted transition rates  $\gamma_{n,m}$  between  $|g\rangle$ ,  $|\downarrow, 1\rangle$ , and  $|\uparrow, 1\rangle$  as a function of  $\varphi$  and mixing chamber temperature  $T$  at  $B = 0\mu\text{T}$ .